DOI: https://doi.org/10.2138/am-2019-6762

Manuscript AM 6762 - Revision 1

On growth and form of etched fission tracks in apatite: a kinetic approach

Raymond Jonckheere*, Bastian Wauschkuhn, Lothar Ratschbacher
Geologie, TU Bergakademie Freiberg, Bernhard-von Cottastraße 2, 09599 Freiberg, Germany

Abstract

We discuss differences between the bulk etch rate ($\boldsymbol{v_B}$) and an alternative radial etch rate ($\boldsymbol{v_R}$) model for fission-track etching in apatite. A skeletal $\boldsymbol{v_R}$-model, based on the inferred orientations of the $\boldsymbol{v_R}$ minima and maxima, accounts for the main geometrical features of etched fission tracks, including the track-surface intersections, track channels and their terminations, and the outlines of confined tracks. It unifies the diverse appearances of etched tracks as variations of a basic plan, governed by the orientation of the etched surface and that of the track. The $\boldsymbol{v_R}$-model also embeds fission-track etching in the mainstream theories of crystal growth and dissolution. However, in contrast to the $\boldsymbol{v_B}$ -model, the $\boldsymbol{v_R}$-model does not provide bottom-up criteria for discriminating between tracks that are counted by an observer or a computer program and those that are not. Moreover, abandoning the $\boldsymbol{v_B}$-model implies that basic assumptions of fission-track dating must be reconsidered, in particular that track counting efficiencies depend only on a critical dip angle, and are thus independent of the track registration geometry and the length distribution.

Keywords

Apatite, fission track, etching, fission-track dating

Introduction

Our understanding of fission-track etching has progressed little since the earliest studies. The still-current bulk etch rate model explains etched-track geometries in terms of the etch rate $\boldsymbol{v_T}$ along the latent-track core and the bulk etch rate(s) $\boldsymbol{v_B}$ of the undamaged detector (Figure 1a; Fleischer and Price 1963a, b; 1964; Tagami and O'Sullivan 2005; Hurford 2019). This model underlies equations relating the number of counted tracks to the number whose etchable section intersects the unetched surface, involving a complex function of $\boldsymbol{v_B}$ and $\boldsymbol{v_T}$ (e.g., Tagami and O'Sullivan 2005):

$$\rho_0 = \rho_L \left\{ 1 - \frac{v_B^2}{v_T^2} + \frac{v_B t_E}{g R_L} \left(1 - \frac{v_B}{v_T} \right) \right\}, \qquad (1)$$

wherein ρ_0 and ρ_L are the observed- and unetched-track densities, R_L the etchable track length, g the geometry factor (½ for external and 1 for internal surfaces), and t_E the etch time. Equation (1) implies that all tracks are counted in surfaces with low bulk etch rates ($\rho_0 \approx \rho_L$ for $\boldsymbol{v_B} \ll \boldsymbol{v_T}$ and $\boldsymbol{v_B}\, t_E \ll R_L$). Equation (1) also has more troubling implications for non-negligible $\boldsymbol{v_B}$. Because it is linear in t_E, it implies an unlimited increase of ρ_0 with increasing etch time. In contrast, the corresponding equation of Jonckheere and Van den haute (1999) has ρ_0 constant for an internal surface (g = 1)[1]:

$$\rho_0 = \rho_L \left\{ 1 - \frac{v_B t_M}{R_L} + \left(\frac{v_B t_M}{2 R_L} \right)^2 \right\}, \qquad (2)$$

wherein t_M is the minimum duration that an added track has to be etched to be identified and counted; if $t_M = 0$ then $\rho_0 = \rho_L$. Equations (1) and (2) differ because the former assumes that a track, once etched, is forever retained and counted, whereas in the latter, a track is eliminated when its lower termination is overtaken by the surface. This illustrates how a wrong assumption can mislead us concerning the relationship between "what is" (ρ_L) and "what is observed" (ρ_0).

[1] Equation (21) of Jonckheere and Van den haute (1999), including the t_M-correction, reformulated in terms of the variables in eq. (1).

This is of some practical interest. The standardless dating methods, based on neutron activation (Jonckheere 2003; Enkelmann et al. 2005; Danhara et al. 2013; Jonckheere et al. 2015; Iwano and Danhara 2018) and on LA-ICP-MS (Hasebe et al. 2004; Hadler et al. 2009; Abdullin et al. 2014; Soares et al. 2014; Gleadow et al. 2015), require an estimate of the counting efficiency $\eta q = \rho_0/\rho_L$. In contrast, the standard-based dating methods (Hurford and Green 1983; Green 1985; Hurford 1998) are not affected if the counting efficiencies ηq of the samples and age standards are identical. However, equation (1) implies that ρ_0/ρ_L increases with decreasing track length R_L. R_L appears in the term that accounts for the addition of tracks due to surface etching (Figure 1c). Of equal concern is the fact that R_L does not appear in the terms referring to tracks intersecting the original surface. This implies that these tracks are counted with efficiencies determined by the critical angle $\theta_C = \arcsin(\boldsymbol{v_B}/\boldsymbol{v_T})$ (Figure 1b), independent of the track-length distribution or the track-registration geometry. This contradicts experimental evidence that ηq depends on both these factors (Jonckheere and Van den haute 2002; Jonckheere 2003). Jonckheere (2003) and Enkelmann et al. (2005) also presented experimental evidence that the track counting efficiencies in external ($\eta q \approx 1.0$) and internal ($\eta q \lesssim 0.9$) prism faces of apatite are not identical, and in the latter case well below the prediction of eq. (1) for a surface with low $\boldsymbol{v_B}$.

Despite the absence of experimental support and disconcerting mathematical properties, the $\boldsymbol{v_B}$-model underpins core assumptions of practical fission-track dating, i.e. that almost lossless track counts can be performed in slow-etching surfaces, and that standard-based ages are unaffected by the different length distributions of the age standard and dated sample. It is therefore relevant to investigate whether the $\boldsymbol{v_B}$-model explains the observed etched-track geometries in apatite. We compare the properties of the bulk-etch rate model ($\boldsymbol{v_B}$-model) with those of a kinetic model of earlier date, the radial etch rate model ($\boldsymbol{v_R}$-model), not before applied to fission tracks but otherwise successful. This shows that in the case of anisotropic etch rates, the two models make different predictions of the etched forms. We then use a skeletal $\boldsymbol{v_R}$-model to calculate the geometries of etched fission tracks in apatite and compare them to microscopic observations. The results lead us to favor the $\boldsymbol{v_R}$-model over the current $\boldsymbol{v_B}$-model and consider the practical implications.

The bulk etch rate $\boldsymbol{v_B}$

The Huygens-Fresnel principle is used for computing the evolution of a specified figure during etching (Spohr 1990). It states that each point on the surface (etch front), exposed at time t, acts as a source of etching in all available (material) directions. The resulting form (etch front) at a later time $t + dt$ is the envelope (tangent) of the combined etch fronts of the individual point sources. Figure 2 illustrates some properties of bulk etching relevant to the present discussion. It is important to distinguish etching of a convex form, which etches from the outside in, and of a concave form, which etches from the inside out. For ease of construction, at this stage, we consider theoretical two-dimensional forms: a circular disc (convex; Figure 2a) and hole (concave; Figure 2c) and a square disc (convex; Figure 2b) and hole (concave; Figure 2d). The circular forms present all orientations (tangents) to the etchant, the extent of each limited to a single point on their circumference. The square forms, in contrast, present four extended orientations, parallel to their sides; all intermediate orientations can be thought of as contracted in the four corner points.

Isotropic bulk etching of a convex form neither eliminates nor adds to the orientations present at the start (Figure 2a, b). In the case of a concave form, it introduces (expands) the "missing", intermediate orientations at discontinuities (corners) of the initial form (Figure 2d, sections 2-3, 4-5, 6-7, 8-1).

The case of anisotropic bulk etching is shown in Figure 2e-h and Figure 3a. The dagger-like inset in each panel of Figure 2e-h is an assumed etch rate plot, i.e. the envelope of the etch rate vectors $\boldsymbol{v_B}$ in all directions of the plane. It is so constructed as to possess mirror symmetries (equal magnitudes in opposite directions) and asymmetries (unequal magnitudes in opposite directions), which are seen to become expressed in the those of the evolving etched shapes. Figure 3a illustrates how the etched shapes are constructed using the Huygens-Fresnel principle (Spohr 1990).

Anisotropic bulk etching adds no new faces to a convex form but eliminates some faces present in the initial form. In the case of a circular initial form, comprising all orientations, those eliminated first are parallel to the line A-B connecting neighboring $\boldsymbol{v_B}$ maxima (Figure 2e). Continued etching eliminates more orientations, corresponding to a symmetrical circle segment centered on the first point. No faces are eliminated from a square form that does not have orientations parallel to the connecting lines between neighboring maxima of the bulk etch rate (A-B in Figure 2f).

These properties are reversed for a concave form: no part of the circumference of the initial form is lost or reduced in size. It is instead split into segments (Figure 2g, h; sections 1-2, 3-4, 4-5, 6-7) at the points where the tangent is parallel to a line connecting neighboring $\boldsymbol{v_B}$-maxima (A-B in Figure 2g, h). At these points, segments parallel to the tangent are inserted, or extended if present from the start (Figure 2g, h; sections 2-3, 5-6, 7-8, 8-1). A concave form does not remain self-similar in the course of etching, but converges towards a shape bounded by faces parallel to the lines connecting neighboring $\boldsymbol{v_B}$-maxima. This implies that we cannot reconstruct the full etch rate plot from a concave etch figure, e.g. a track cross-section (Yamada et al. 1993), just its envelope.

The radial etch rate $\boldsymbol{v_R}$

An isotropic-$\boldsymbol{v_B}$ model with low $\boldsymbol{v_T}$ accounts for the cone-shaped tracks with circular or elliptical surface intersections in isotropic materials (glasses and plastics; Fleischer and Price 1963a; b). An anisotropic-$\boldsymbol{v_B}$ model with high $\boldsymbol{v_T}$ goes some way towards explaining needle-shaped track channels with polygonal surface intersections in minerals (Fleischer and Price 1964; Maurette 1966). Researchers investigating defects in semiconductors and other crystalline materials by means of etching also reported polygonal etch figures (Batterman 1957; Lovell 1958; Holmes 1959), but proposed a different kinetic model (Irving 1959; Frank and Ives 1960; Jaccodine 1962). Their model is based on the radial etch rate $\boldsymbol{v_R}$, i.e. the rate at which a plane is displaced parallel to itself. An isotropic-$\boldsymbol{v_R}$ model gives the same results as an isotropic-$\boldsymbol{v_B}$ model for both convex and concave forms (Figure 2a-d). An anisotropic-$\boldsymbol{v_R}$ model, in contrast, predicts a different evolution of both convex (Figure 2i, j) and concave (Figure 2k, l) forms than an anisotropic-$\boldsymbol{v_B}$ model. Figure 3b illustrates how the etched shapes are constructed using the definition of the radial etch rate.

In contrast to the anisotropic-$\boldsymbol{v_B}$ model (Figure 2e, f), the anisotropic-$\boldsymbol{v_R}$ model (Figure 2i, j) predicts that a convex form develops flat faces perpendicular to the $\boldsymbol{v_R}$-maxima, even if these are not present in the initial form. In Figure 2i, the tangent C-D is perpendicular to a local $\boldsymbol{v_R}$-maximum (dagger-like inset in the center of the Figure 2i). Following the definition of radial etch rate, displacing C-D parallel to itself a distance proportional to the magnitude of the perpendicular etch rate vector gives rise to the edge 2-3 of the etched form. The sections 1-2 and 4-1 are perpendicular to other $\boldsymbol{v_R}$-maxima. Section 3-4 remains curved because it has no tangent perpendicular to a local $\boldsymbol{v_R}$-maximum. The same faces develop from the four corners of a square initial form (Figure 2j).

In the case of a concave form, flat faces develop perpendicular to cusp-like $\boldsymbol{v_R}$-minima (Figure 2k, l; sections 2-3, 5-6) and curved faces opposite smooth $\boldsymbol{v_R}$-minima (Figure 2l; section 7-1). As etching proceeds, flat faces expand and the curvature of others decreases, creating distinct corners at intersections. The anisotropic-$\boldsymbol{v_R}$ model thus allows for faces of finite extent to be created as well as eliminated. A law of least action determines the relative extent of the faces, i.e. the integral over all orientations of the product of $\boldsymbol{v_R}$ and the surface area dS it acts on is minimized (Jaccodine 1962), minimizing free energy. Common fission-track etching protocols enlarge the track cross-sections a hundredfold, so that most orientations are eliminated and etched tracks are bounded by nearly flat faces, although these must not be perfectly flat, even after prolonged etching.

There is substantial experimental evidence that the $\boldsymbol{v_R}$-model accurately predicts the etching of convex (spheres, cylinders) and concave (cylindrical grooves, hemispherical hollows) forms. This has been demonstrated for crystals of germanium, iron, silica, lithium fluoride, rutile, and quartz (Batterman 1957; Irving 1959; 1960; Holmes 1959; Frank and Ives 1960; Ives and Hirth 1960; Jaccodine 1962; Heimann 1971; Spink and Ives 1971; Heimann et al. 1973). The same mechanism, with $\boldsymbol{v_R}$ as the growth rate of a crystal plane instead of its etch rate, also describes crystal growth. In contrast, the anisotropic-$\boldsymbol{v_B}$ model for fission-track etching has not been put to an empirical test but appears to be an ad hoc extension of the isotropic-$\boldsymbol{v_B}$ model for glass and plastics.

The atomistic approach

A theoretical advantage of the anisotropic $\boldsymbol{v_R}$-model is that it addresses the root cause of the difference between isotropic and anisotropic etching, whereas the anisotropic $\boldsymbol{v_B}$-model merely reflects its outward expression. The crucial difference between isotropic and anisotropic materials is that the latter possess preferential orientations, which isotropic materials do not. The

DOI: https://doi.org/10.2138/am-2019-6762

relevant orientations in this context are those of so-called periodic bond chains (Hartman and Perdok 1955), i.e. straight chains of lattice atoms that are most resistant to being broken by the etchant. This concept implies the distinction between kinked (K) faces that contain no such orientation, stepped (S) faces that contain one, and flat (F) faces that contain two or more (Figure 4). It furthermore fixes the order of their radial etch rates for equal bond strengths ($\boldsymbol{v_R(F)} < \boldsymbol{v_R(S)} < \boldsymbol{v_R(K)}$). The kinetic etch model and periodic bond chains go back to before fission-track dating, but are well established and based on consistent theories (Woensdrecht 1993; Chernov 2004; Woodruff 2015).

Jonckheere and Van den haute (1996) identified F-, S-, and K-faces with pitted, scratched, and textured faces, a distinction based on optical-microscope observations of etched tracks in titanite (Gleadow 1978). In apatite, the basal face is an F-face and prism faces are S-faces; other faces are K-faces, as far as we can tell. Because of the six-fold axis perpendicular to the basal face, it contains three periodic bond chains rotated 120°. The prism face contains just one, parallel to the ***c***-axis. In an idealized lattice, a cross-section parallel to the periodic bond chain in an S-face (Figure 4b; A-B) is similar to one parallel to a periodic bond chain in an F-face (Figure 4a; A-B), and a cross-section perpendicular to the periodic bond chain in an S-face (Figure 4b; B-C) is similar to one through a K-face (Figure 4c; B-C). In apatite, a prism face (S) would thus be comparable to a basal face (F) parallel to the ***c***-axis and to a textured (K) perpendicular to the ***c***-axis. One consequence is that etch pits in a basal face widen in all surface directions (Figure 4a), but those in prism faces grow parallel to the ***c***-axis (Figure 4b). There appears to be no comparable mechanism for etch-pit growth textured faces (Figure 4c). In this sense, an etched track in a prism face can thus be thought of as equivalent to one in a basal face flattened perpendicular to the ***c***-axis. A familiar expression of the same notion is the fact that etched polishing scratches in a prism face are broad perpendicular to the ***c***-axis, as in a basal face, and narrow parallel to the ***c***-axis.

The model surface track

The model (or prototype) surface track is a direct result of the properties of the anisotropic-$\boldsymbol{v_R}$ model, i.e. that fast-etching faces develop at convex intersections and slow-etching faces at concave intersections. For a first approximation, it is thus sufficient to locate the convex and concave intersections. Following a short interval of etching at high $\boldsymbol{v_T}$ and negligible $\boldsymbol{v_R}$ the damaged track core is drained of defects, and the latent track leaves a narrow, submicroscopic channel (Figure 5a), whose further development is governed by $\boldsymbol{v_R}$ alone. Its longitudinal cross-section is convex at its intersection with the surface and concave at its lower termination (Figure 5b). Thus, fast-etching faces develop at the track-surface intersection and slow-etching faces at its endpoint. A transverse cross-section through the track channel is concave, and thus bounded by the slowest-etching faces parallel to the track axis (Figure 5c). This gives rise to a dual track, comprising a track channel and a distinct etch pit at its surface intersection. The etch pit walls are fast-etching faces hinged on the slowest-etching orientations in the surface, reflecting the fact that the etch pit is concave parallel to the surface and convex perpendicular to it. Figure 6 shows an etch pit at a dislocation in a basal apatite surface; the hillocks on the etch-pit walls confirm that they are fast etching (cosine rule; Irving 1962; Jonckheere and Van den haute 1996).

The polar etch rate plot

The length and orientation of the latent track and the specific radial etch rates of the surface and surrounding material produce modifications of the model etched track. We make some assumptions in order to investigate their effects and to construct etched-track geometries for specific cases. Our main assumption is that the radial etch rates of the basal and prism faces of apatite are minima. This is warranted on the basis that the basal face is an F face and prism faces are S faces (Jonckheere and Van den haute 1996). In the absence of periodic bond chains other than those parallel and perpendicular to the ***c***-axis, all other faces are fast-etching K faces. It follows that the radial etch rate is maximum in one such direction. We assume that this is at ca. 30° to the ***c***-axis. This produces etch pit faces dipping 30° with respect to the basal plane, as indicated by the etched-track profiles in an apatite basal face (Figure 1 of Alencar et al. 2015). Our final assumption is one of convenience: we set the magnitudes of $\boldsymbol{v_R}$ in all other orientations at the maximum values that do not produce additional or curved etch-pit faces (Figure 7a). These magnitudes can be calculated using the cosine rule (Irving 1962; Jonckheere and Van den haute 1996). This leaves undetermined the relative etch rates of different prism faces. We assume a hexagonal pattern, with little variation between prism faces, as all are S faces containing periodic bond chains along the ***c***-axis (Figure 7b). An exact calculation of etched-track geometries requires numerical values for the full etch rate plot, i.e. the magnitude of $\boldsymbol{v_R}$ in all directions. Such data are lacking; the values would moreover depend on the etching conditions. Our present aim is more limited, i.e. to demonstrate that, in contrast to the current anisotropic-$\boldsymbol{v_B}$ model, the anisotropic-$\boldsymbol{v_R}$ model produces predictions of the etched-track geometries in specific cases that are in agreement with microscope observations. The $\boldsymbol{v_R}$ maxima and minima are enough for this purpose.

The intrinsic radial etch rate of a given crystallographic plane is determined by its orientation relative to the periodic bond chains. Periodic bond chains are most resistant to being broken by the etchant, but not to being etched from their ends. This implies that the nature (F, S, K) of a given crystallographic plane, and therefore its etch rate, is not the same where it intersects an external crystal face or polished surface as the intrinsic radial etch rate of the same continuous, unbroken plane. An important practical consequence is that one cannot confidently infer radial shift velocities from the size and shape of etch pits at the track intersections with the etched surface.

Figure 8a shows the etch pit and channel of a track perpendicular to an apatite basal face. Figure 8b plots the rate of etch pit growth as a function of orientation. The solid sections are reconstructed from the etch pit outline. The dashed sections are the minimum etch rates required for the etch pit to present no edges or curvature other than those observed. The central track channel is bounded on six sides by faces parallel to the ***c***-axis and to the etch pit edges. The variation of their etch rates with orientation is thus as in Figure 8b but scaled down. However, neither of these values should be interpreted as the intrinsic radial etch rate of an external prism face. The plotted values in Figure 8b represent the rate of retreat of surface steps parallel to the periodic bond chains in a basal plane. They are thus not the etch rates of plane surfaces, as required by the anisotropic-$\boldsymbol{v_R}$ model, but should instead be interpreted as projections of the etch rates of the etch pit faces on the basal plane. Faces containing periodic bond chains parallel and perpendicular to the ***c***-axis (Figure 9a) bound a track channel perpendicular to the basal plane. This is not the case for low-index external prism faces. As Honess (1927) reported, and measurement confirms, the etch pit edges in the basal face are rotated ~15° with respect to the low-index prism faces. This underscores the risks of inferring surface etch rates from the dimensions of etch figures.

DOI: https://doi.org/10.2138/am-2019-6762

Figure 8c shows the openings of tracks perpendicular to the ***c***-axis in an external prism surface. Figure 8d shows the etch rate plot derived from their outlines. The etch rates perpendicular to the straight edges of the track opening are shown in solid line. The etch rates in all other orientations, in dashed line, are minimum values that do not introduce sides or curvature other than those observed. The etch-rate minima are perpendicular to the long sides (A-B and D-E) and thus to the ***c***-axis. This agrees with the fact that A-B and D-E are bound by periodic bond chains parallel to the ***c***-axis (Figure 9b). The high etch rates of the rhombic prisms (B-C-D; E-F-A) appear inconsistent with the etch-rate minimum perpendicular to the basal plane (Figure 7a), reflecting the effect of periodic bond chains on the etch rate of the basal plane (Figure 9b). The solution lies in the fact that, by definition, periodic bond chains are the most resistant to being broken by the etchant but not to being consumed from their ends. Thus, periodic bond chains parallel to the basal plane emerging at a prism surface do not exert their normal resistance to the etchant, lifting the minimum perpendicular to the basal plane in Figure 7a. On this condition, the empirical etch rate plot based on the outline of the track openings in an etched prism surface (Figure 8d) is consistent with that assumed on general principle (Figure 7a). The empirical plot based on the rate of etch pit growth in the basal plane (Figure 8b) is also consistent with the radial etch rate plot (Figure 7b). The specific reason in this case is that the periodic bond chains parallel to the ***c***-axis emerge at the basal surface, allowing them to be etched from their ends.

This demonstrates that inferring etch rates from etched-track geometries (Gleadow 1981; Durrani and Bull 1987; Villa et al. 1997; Yamada et al. 1994; Gleadow et al. 2002; Sobel and Seward 2010) is fraught with danger. Etch pit outlines are on the whole inappropriate for this purpose. In contrast, the track channels farther from the surface are free from the effect of dangling periodic bond chains, but less accessible to detailed observation and measurement. Track channels perpendicular to the ***c***-axis are the most useful for determining important etch rates because they are confined between a pair of prism faces and a pair of basal faces, each parallel to specific periodic bond chains (Figure 9b). Any track at an angle to the ***c***-axis is confined between a pair of prism faces but not between basal faces (Figure 9c). This gives rise to their distinctive knife-blade shape (Gleadow 1981), with the exception of tracks nearly parallel or perpendicular to the ***c***-axis.

This is a preprint, the final version is subject to change, of the American Mineralogist (MSA)
Cite as Authors (Year) Title. American Mineralogist, in press.
DOI: https://doi.org/10.2138/am-2019-6762

Calculated track geometries

Although an exact solution is not attainable at this stage, we use the provisional etch rate plot to calculate the main geometrical features of tracks etched in a basal, a prism, and an intermediate apatite surface. Figure 10 shows the calculated surface intersection of a track dipping 60° in a plane perpendicular to a basal (Figure 10a, b), prism (Figure 10d, e), and an intermediate surface (Figure 10g, h). The appendices show results for other dip angles (Figure A1: basal surface; Figure A2: prism surface; Figure A3: intermediate surface). In all cases, the etched shape consists of three parts: the track channel A-B-C-D, the surface layer removed by etching P-Q-R-S, and an etch pit X-Y-Z. The channel is knife-blade shaped, except when the track is parallel or perpendicular to the ***c***-axis (Figures A1-A3). The etch rates $\boldsymbol{v_R}$ perpendicular to the track axis determine its height and width. An etch pit is a prominent feature of the basal face, foremost for reason that it expands in all surface directions (Figure 10a, b). Its diameter and depth are little influenced by the dip angle of the track, except at low values, at which the diameter increases and the depth decreases somewhat (Figure A1). The etch pit outline and dimensions are nevertheless fairly uniform. The channel connects to the apex of the etch pyramid if the track is perpendicular to the surface and to the lower part of an etch pit face for lesser dip angles. The channel-etch pit intersection is an upright slit of almost constant width but variable height depending on the dip of the track. These properties are in good qualitative agreement with observations (Figure 10c).

The track channel in a prism face has the characteristic knife-blade shape (Figure 10d, e), except when the track is more or less perpendicular to the ***c***-axis, and confined between a pair of basal planes. An etch pit develops at its intersection with the surface, but it is flat in the direction perpendicular to the ***c***-axis because, like the channel, it is confined between a pair of prism planes. As its dip decreases, the channel broadens parallel to ***c***, and encloses the etch pit (Figure A2). It is for this reason that the etch pit is a much less distinct feature of tracks in a prism face than in a basal face. The formation of an etch pit is however also the reason that the surface openings of tracks in a prism surface are more or less the same size in the direction of ***c***. Tracks with shallow dip angles and azimuth orientations subparallel to ***c*** can however have somewhat larger track openings (Figure A2). This could explain some of the variation of Dpar (etch pit length) values, and its dependence on track orientation (Sobel and Seward 2010), although other factors might contribute. The extent to which this is the case depends on the details of the radial etch rate plot. Figure 10f illustrates the needle-like channels and distinct etch pits of tracks at high azimuth angles to ***c*** (A), the prominent knife-blade shaped tracks without distinguishable etch pits in other directions, except subparallel to the ***c***-axis where the knife-blade shape is seen edge-on (B).

The intermediate case is represented by a surface at 45° to the ***c***-axis (Figure 10g, h). The tracks have the common dual structure, made up of a knife-blade shaped channel and an etch pit. The latter is not well developed as most of it is located within the surface layer removed by etching and another part is enclosed within the channel. A small collar can nevertheless develop at the surface intersection of tracks parallel to slow-etching planes, which have a narrow channel (Figure A3). Due to the lesser importance of the etch pit, the variation in channel width is directly expressed at the surface, so that the size of the track openings varies within wide margins, depending on the track dip angle, the surface orientation, and the details of the radial etch rate plot. Figure 10i shows a representative surface, in which the track openings exhibit minor additional structure (A). The size of the track openings is uniform because the (ion-) tracks are parallel.

The track ends present no preferential orientations; therefore, the complete radial etch rate plot is relevant. The calculated geometries show that the tracks are terminated by faces parallel and perpendicular to the basal plane (Figure 11). This implies that the length of surface tracks decreases with etch time, although, depending on their orientation and the actual etch rates, the shortening can be small to negligible for tracks etched in a basal or prism surface. Jonckheere and Van den haute (2002) calculated the mean full length of fossil tracks in Durango apatite from the projected-length distribution of surface tracks. Their results for the basal surface (13.9 ± 0.2 μm), prism surface (13.8 ± 0.2 μm), and intermediate (textured) surface (12.5 ± 0.2 μm) indeed seem to indicate an underestimation compared to the mean length of confined tracks (14.4 ± 0.1 μm) that correlates with the relative surface etch rates (Jonckheere and Van den haute 1996).

Confined tracks offer a further test of an etch model. Those at high angles to the ***c***-axis that deviate from the knife-blade shape are the most diagnostic. The intersections of tracks at 90-60° to the ***c***-axis (Figure 12a, b, c), calculated with the etch rate plot in Figure 7, compare well with

DOI: https://doi.org/10.2138/am-2019-6762

observed tracks (Figure 12d, e, f). Those almost perpendicular to $\boldsymbol{c}$ have narrow channels with a pyramid on either side of the host track or cleavage (Figures 12a, d). At somewhat lesser angles to $\boldsymbol{c}$, the channel broadens but the tracks retain the distinct pair of etch pyramids (Figures 12b, e). At still lesser angles, the characteristic knife-blade shape obscures the etch pyramids (Figures 12c, f). The tracks in Figure 12 resemble the fragmented types F2 (Figure 12a), F1 (Figure 12b), and blade type (Figure 12c) of Hejl (1995). Our model attributes their specific morphologies to anisotropic etching ($\boldsymbol{v_R}$), and not to discontinuous etching of the damage along the latent track ($\boldsymbol{v_T}$).

In accordance with the anisotropic-$\boldsymbol{v_R}$ model, the confined track in Figure 12f has a prominent basal plane (B) at each end. The prism plane (P) is less well-developed and curved, indicating that the etch rate plot (Figure 7) is inaccurate in certain details. This is not unexpected as it was deliberately simplified and constructed to avoid complications due to curvature of the developing faces. Curvature can however be introduced ad hoc by reducing the radial etch rates in certain directions (Figure 11h, i, j). On the one hand, this indicates, that, with fine-tuning, an anisotropic-$\boldsymbol{v_R}$ model can deal with more complex track shapes than those considered here, that are not made up of flat faces. On the other hand, it means that step-etching of confined tracks might provide a means of determining the numerical values of the radial etch rates in most relevant directions.

Implications and outlook

The anisotropic-$\boldsymbol{v_B}$ model has existed almost unchanged for over five decades in the recesses of the fission-track method. One of its implications is that fission tracks can be counted without significant losses in slow-etching surfaces, such as apatite prism faces (Gleadow 1981) and muscovite cleavage planes (Belyaev et al. 1980; Khan 1980). Another is that track counting efficiencies are not relevant to the standard-based dating methods (Hurford and Green 1983; Green 1985). We submit that the anisotropic-$\boldsymbol{v_B}$ model cannot account for the observed track geometries in apatite, and should be laid to rest. We suggest that it be replaced with an anisotropic-$\boldsymbol{v_R}$ model based on the radial etch rate (radial shift velocity). This embeds track etching in the mainstream kinetic theories of crystal growth and dissolution, based on the seminal studies of Burton et al. (1951) and Frank (1958), and buttressed by the atomistic theory of Hartman and Perdok (1955) with roots stretching back to the fundamental concepts of Kossel (1927) and Stranski (1928).

Our application of the anisotropic-$\boldsymbol{v_R}$ model to fission-track etching in apatite has produced results that recommend it. It accounts for the complex etched-track geometries and unifies their varied manifestations as variations on a theme depending on the relative size and orientation of the surface layer removed by etching, the etch pit at the track-surface intersection, and the track channel. The anisotropic-$\boldsymbol{v_R}$ model for fission-track etching in apatite is at this stage qualitative, based on assumptions concerning the orientation of the etch-rate minima and maxima, and the further assumption that the intermediate etch rates have no effect on the etched-track geometries. Detailed etch rate measurements must flesh out this skeletal model, and allow to calculate the exact shape of an etched fission track in any specified surface, with any orientation and at any etch time. Comparison with experiments must then validate the model or reveal the need for improvements. Graphics algorithms can be applied for determining the appearance of the etched tracks under an optical microscope. A discrimination problem must then be addressed, i.e. establishing observer- or software-specific criteria for distinguishing between tracks and non-tracks.

Does this serve a practical purpose? The end of the anisotropic-$\boldsymbol{v_B}$ model would put an end to its doubtful implications, that short tracks are counted with greater efficiency than long tracks, and that all tracks maintain a constant (axial) length and remain countable, leading to an unlimited increase of ρ_0/ρ_L with etching time (eq. (1); Tagami and O'Sullivan 2005). A bottom-up understanding of which tracks are counted and which are not will serve to validate the empirical track counting efficiencies (ηq factors) used with the neutron-activation based, standardless dating methods (Jonckheere 2003; Enkelmann et al. 2005; Jonckheere et al. 2015; Danhara and Iwano 2013; Wauschkuhn et al. 2015; Iwano et al. 2018). In the same manner, it will allow us to evaluate the ad hoc experimental factors (k for the ε-method, Hasebe et al., 2004; α for the ξ-method; Gleadow et al., 2015), assumed for absolute dating with the LA-ICP-MS-based fission-track methods. In contrast to the anisotropic-$\boldsymbol{v_B}$ model, the anisotropic-$\boldsymbol{v_R}$ model implies that the etchable lengths of surface tracks decrease with etch time. Thus short tracks can become unrecognizable and, in the end, invisible under the microscope. A population containing an excess of short tracks must thus not be counted with the same efficiency as one containing only long tracks, as in age standards. If confirmed, this implies that the standard-based dating methods (Z- and ζ-methods; Hurford and Green 1983; Green 1985) are less than accurate. A lengthdependent threshold can have a significant effect on the track counts (Jonckheere and Van den haute 2002).

Following earlier attempts (Keil et al. 1987; Wagner et al. 1989; Wagner and Hejl 1991), computerized microscopes will prompt renewed efforts to extract thermal histories from the length statistics of surface tracks. This will place track etching in the forefront, as the new methods will have to reckon with two main factors. (1) A track length decrease with etch time predicted by the anisotropic-$\boldsymbol{v_R}$ model. (2) An opposed increase due to residual damage at the latent-track extremities, which etches at a reduced track etch rate $\boldsymbol{v_T}$ (Jonckheere et al. 2017) but was not considered here.

Acknowledgments

Research funded by the German Science Foundation (DFG) under JO 358/3-1 and JO 358/4-1. We are indebted to Richard Ketcham and Sandro Guedes for their insightful and constructive reviews.

References

Abdullin, F., Solé, J., and Solari, L. (2014) Fission-track dating and LA-ICP-MS multi-elemental analysis of the fluorapatite from Cerro de Mercado (Durango, Mexico). Revista Mexicana de Ciencas Geologicas 31, 395–406 (in Spanish).

Alencar, I., Guedes, S., Palissari, R., and Hadler, J.C. (2015) On the influence of etch pits in the overall dissolution rate of apatite basal sections. Physics and Chemistry of Minerals 42, 629–640.

Batterman, B.W. (1957) Hillocks, pits and etch rate in Germanium crystals. Journal of Applied Physics 28, 1236-1241.

Belyaev, A.D., Bahromi, I.I., Beresina, N.V., Bikbova, Z.S., Volkova, N.I., Gorevoi, A.A., Kogan, V.I., Muminov, A.I., Pikul, V.P., and Usmandiarov, A.M. (1980) Critical angles for fission fragment registration in some solid state track detectors. Nuclear Tracks 4, 49 52.

Burton, W.K., Cabrera, N., and Frank F.C. (1951) The growth of crystals and the equilibrium structures of their faces. Philosophical Transactions of the Royal Society of London A243, 299-358.

Chernov, A.A. (2004) Notes on interface growth kinetics 50 years after Burton, Cabrera and Frank. Journal of Crystal Growth 264, 499–518.

Danhara, T., and Iwano, H. (2013) A review of the present state of the absolute calibration for zircon fission track geochronometry using the external detector method. Island Arc 22, 264–279.

Durrani, S.A., and Bull, R.K. (1987) Solid State Nuclear Track Detection. Principles, Methods and Applications. International Series in Natural Philosophy 111. Pergamon Books Ltd., Oxford, pp.304.

Enkelmann, E., Jonckheere, R., and Wauschkuhn, B. (2005) Independent fission-track ages (ϕ-ages) of proposed and accepted apatite age standards and a comparison of ϕ-, Z-, ζ- and ζ_0-ages: implications for method calibration. Chemical Geology 222, 232–248.

Fleischer, R.L., and Price, P.B. (1963a) Tracks of charged particles in high polymers. Science 140, 1221-1222.

Fleischer, R.L., and Price, P.B. (1963b) Charged particle tracks in glass. Journal of Applied Physics 34, 2903-2904.

Fleischer, R.L., and Price, P.B. (1964) Techniques for geological dating of minerals by chemical etching of fission fragment tracks. Geochimica et Cosmochimica Acta 28, 1705-1714.

Frank, F.C. (1958) On the kinematic theory of crystal growth and dissolution processes. In T.H. Doremus, B.W Roberts and D. Turnbull, Eds., Growth and Perfection of Crystals, Wiley, London, U.K., p. 411-419.

Frank, F.C., and Ives, M.B. (1960) Orientation-dependent dissolution of Germanium. Journal of Applied Physics 31, 1996-1999.

Gleadow, A.J.W. (1978) Anisotropic and variable track etching characteristics in natural sphenes. Nuclear Track Detection 2, 105-111.

Gleadow, A.J.W. (1981) Fission track dating methods: what are the real alternatives? Nuclear Tracks 5, 3-14.

Gleadow, A.J.W., Belton, D.X., Kohn, B.P., and Brown, R.W. (2002) Fission track dating of phosphate minerals and the thermochronology of apatite. In M. J. Kohn, et al., eds. Phosphates, Geochemical, Geobiological, and Materials Importance, 48, p. 579–630. Reviews of Mineralogy and Geochemistry Mineralogical Society of America, Chantilly, Virginia.

Gleadow, A., Harrison, M., Kohn, B., Lugo-Zazueta, R., and Phillips, D. (2015) The Fish Canyon Tuff: a new look at an old low-temperature thermochronology standard. Earth and Planetary Science Letters 424, 95–108.

Green, P.F. (1985) Comparison of zeta calibration baselines for fission-track dating of apatite, zircon and sphene. Chemical Geology (Isotope Geoscience Section) 58, 1-22.

Hadler, J.C., Iunes, P.J., Tello, C.A., Chemale, F. Jr., Kawashita, K., Curvo E.A.C., Santos, F.G.S., Gasparini T.E., Moreira P.A.F.P., and Guedes S. (2009) Experimental study of a methodology for fission-track dating without neutron irradiation. Radiation Measurements 44, 955–957.

Hartman, P., and Perdok, W.G. (1955) On the relation between structure and morphology of crystals I. Acta Crystallografica 8, 49–52.

Hasebe, N., Barbarand, J., Jarvis, K., Carter, A., and Hurford, A.J. (2004) Apatite fission-track chronometry using laser ablation ICP-MS. Chemical Geology 207, 135–145.

Heimann, R., Franke, W., and Lacmann, R. (1971) Dissolution forms of single crystal spheres of rutile. Journal of Crystal Growth 13/14, 202-206.

Heimann, R., Franke, W., and Lacmann, R. (1975) The dissolution forms of single crystal spheres. IV. Dissolution of MgO. Journal of Crystal Growth 28, 151-156.

Hejl, E. (1995) Evidence for unetchable gaps in apatite fission tracks. Chemical Geology (Isotope Geoscience Section) 122, 259-269.

Holmes, P.J. (1962) Practical applications of chemical etching. In P.J. Holmes, Ed., The Electrochemistry of Semiconductors,. Academic Press, London, 329-377.

Honess, A.P. (1927) The Nature, Origin and Interpretation of the Etch Figures on Crystals. Wiley, New York, pp. 171.

Hurford, A.J. (1998) Zeta: the ultimate solution to fission-track analysis calibration or just an interim measure? In Van den haute, P., De Corte, F., Eds., Advances in Fission-Track Geochronology. Kluwer Academic Publishing, Netherlands, pp. 19-32.

Hurford, A.J. (2019) An historical perspective on fission-track thermochronology. In M.G. Malusà and P.G. Fitzgerald, Eds., Fission-Track Thermochronology and its Application to Geology. Springer Textbooks in Earth Sciences, Geography and Environment. Springer International Publishing AG, 3-23.

Hurford, A.J., and Green, P.F. (1983) The zeta age calibration of fission track dating. Isotope Geoscience 1, 285–317.

Irving, B.A. (1959) Shapes of etch hillocks and pits and their correlation with measured etch rates. Journal of Applied Physics 31, 109-111.

Irving, B.A. (1962) Chemical etching of semiconductors. In P. J. Holmes, Ed., The Electrochemistry of Semiconductors. Academic Press, London, 256–289.

Ives, M.B., and Hirth, J.P. (1960) Dissolution kinetics at dislocation etch pits in single crystals of lithium fluoride. The Journal of Chemical Physics 33, 517-525.

Iwano, H., Danhara, T., and Hirata T. (2018) Standardless fission-track ages of the IUGS age standards. Chemical Geology 488, 87–104.

Jaccodine, R.J. (1962) Use of modified free energy theorems to predict equilibrium growing and etching shapes. Journal of Applied Physics 33, 2643–2647.

Jonckheere, R. (2003) On the ratio of induced fission-track densities in a mineral and a co-irradiated muscovite external detector with reference to fission-track dating of minerals. Chemical Geology 200, 41–58.

Jonckheere, R., and Van den haute, P. (1996) Observations on the geometry of etched fission tracks in apatite: implications for models of track revelation. American Mineralogist 81, 1476–1493.

Jonckheere, R., and Van den haute, P. (1999) On the frequency distributions per unit area of the projected and etchable lengths of surface-intersecting fission tracks: influences of track revelation, observation and measurement. Radiation Measurements 30, 155-179.

Jonckheere, R., and Van den haute, P. (2002) On the efficiency of fission-track counts in an internal and external apatite surface and in a muscovite external detector. Radiation Measurements 35, 29–40.

Jonckheere, R., Van den haute, P., and Ratschbacher, L. (2015) Standardless fission-track dating of the Durango apatite age standard. Chemical Geology 417, 44–57.

Jonckheere, R., Tamer, M.T., Wauschkuhn, B., Wauschkuhn, F., and Ratschbacher, L. (2017) Single-track length measurements of step-etched fission tracks in Durango apatite: "Vorsprung durch Technik". American Mineralogist 102, 987–996.

Keil, R., Pahl, M., and Bertagnolli, E. (1987) Thermal history and length distribution of fission tracks: part II. Nuclear Tracks and Radiation Measurements 13, 25-34.

Khan, H.A. (1980) Track registration and development efficiencies of solid state nuclear track detectors. Nuclear Instruments and Methods 173, 43-54.

Kossel, W. (1927) On the theory of crystal growth. Nachrichten von der Gesellschaft der Wissenschaften zu Göttingen 2, 135–143 (in German).

Lovell, L.C. (1958) Dislocation etch pits in apatite (letter to the editor). Acta Metallurgica 6, 775-778.

Maurette, M. (1966) Investigation of heavy-ion tracks in natural minerals of terrestrial and extra-terrestrial origin. Bulletin de la Société Française de Minéralogie et Cristallographie 89, 41-75 (in French).

Spink, G.M., and Ives M.B. (1971) Morphology of Crystallographic Etch Pits in Iron. Journal of Applied Physics 42, 511-516.

Soares, C.J., Guedes, S., Hadler, J.C., Mertz-Kraus, R., Zack, T., and Iunes, P.J. (2014) Novel calibration for LA-ICP-MS-based fission-track thermochronology. Physics and Chemistry of Minerals 41, 65–73.

Sobel, E.R., and Seward D. (2010) Influence of etching conditions on apatite fission-track etch pit diameter. Chemical Geology 271, 59–69.

Spohr, R. (1990) Ion Tracks and Microtechnology. Principles and Applications. Friedrich Vieweg & Sohn Verlagsgesellschaft mbH, Braunschweig, pp. 272.

Stranski, I.N. (1928) The theory of crystal growth. Zeitschrift für Physik und Chemie 136, 259–278.

Tagami, T., and O'Sullivan, P.B. (2005) Fundamentals of fission-track thermochronology. In P.W. Reiners, and T.A. Ehlers, Eds., Low-temperature Thermochronology: Techniques, Interpretations, and Applications, 58, p. 19-47. Reviews in Mineralogy and Geochemistry Mineralogical Society of America, Chantilly, Virginia..

Villa, F., Grivet, M., Rebetez, M., Dubois, C., and Chambaudet, A. (1997) Calibration and simulation of apatite fission track etching: influence of diffusion and crystal symmetry. Radiation Measurements 28, 543-548.

Wagner, G.A., Gleadow, A.J.W., and Fitzgerald, P.G. (1989) The significance of the partial annealing zone in apatite fission-track analysis: projected track length measurements and uplift chronology of the Transantarctic Mountains. Chemical Geology (Isotope Geoscience Section) 79, 295-305.

Wagner, G.A., and Hejl, E. (1991) Apatite fission-track age-spectrum based on projected track-length analysis. Chemical Geology (Isotope Geoscience Section) 87, 1-9.

Wauschkuhn, B., Jonckheere, R., and Ratschbacher, L. (2015) The KTB apatite fission-track profiles: building on a firm foundation? Geochimica et Cosmochimica Acta 167, 27–62.

Woensdregt, C.F. (1993) Hartman-Perdok Theory: influence of crystal structure and crystalline interface on crystal growth. Faraday Discussions 95, 97-107.

Woodruff, D.P. (2015) How does your crystal grow? A commentary on Burton, Cabrera and Frank (1951) 'The growth of crystals and the equilibrium structure of their surfaces'. Philosophical transactions of the Royal Society A373, 1-11.

Yamada, R., Tagami, T., and Nishimura S. (1993) Assessment of overetching factor for confined fission-track length measurement in zircon. Chemical Geology (Isotope Geoscience Section) 104, 251-259.

Figure captions

Figure 1. Track etching according to the $\boldsymbol{v_B}$ -model: $\boldsymbol{v_B}$: bulk etch rate; $\boldsymbol{v_T}$: track etch rate; t_E: etch time; θ_C = arcsin($\boldsymbol{v_B}/\boldsymbol{v_T}$): critical angle for track revelation (after Tagami and O'Sullivan, 2005). a: a steep-dipping surface track etched as a cone; b: a track dipping at less than the critical angle; c: a track added as a result of bulk etching of the surface. Below the figure is the equation of Tagami and O'Sullivan (2005), with arrows relating its different terms to the various track types (a-c).

Figure 2. Etching of idealized two-dimensional convex and concave shapes. The circumference of the circular starting forms comprises all orientations of the plane (tangents) with equal, infinitesimal extent. The square forms are bounded by two extended orientations, with all intermediate orientations contracted in the vertices. a-d: isotropic bulk etch rate ($\boldsymbol{v_B}$) and isotropic radial etch rate ($\boldsymbol{v_R}$) model; e-h: anisotropic bulk etch rate model; i-l: anisotropic radial etch rate model. The inset in the center of each panel represents the variation of the etch rate with orientation.

Figure 3. Anisotropic etching of a convex form ABC according to (a) the bulk etch rate ($\boldsymbol{v_B}$-) and (b) the radial etch rate ($\boldsymbol{v_R}$-) model. The etch rate plot is the same in (a) and (b), but the etched shapes differ because the $\boldsymbol{v_B}$ and $\boldsymbol{v_R}$ have a different meaning. In the $\boldsymbol{v_B}$-model (a), each point etches in all material directions (shaded sectors of the etch rate plots), and the displacement of the straight edges A-B and B-C is governed by the etch rates whose projection normal to A-B and B-C is greatest (arrows). The corner B is a point like another along A-B and B-C. In the $\boldsymbol{v_R}$-model (b), the etch rate is the rate of displacement of a flat face as a whole, controlled only by the etch rate perpendicular to that face (arrows). The corner B at the intersection of A-B and B-C comprises all orientations intermediate between those of A-B and B-C, and the corresponding etch rates compete (shaded area of the etch rate plot). In this example, only the face develops that has the greatest $\boldsymbol{v_R}$ (arrow). In cases with less pronounced etch rate maxima, other faces can develop as well.

Figure 4. Different surfaces of an idealized regular lattice (Kossel, 1927) of periodic bond chains (Hartman and Perdok, 1955). a: a flat face (F) contains two or more periodic bond chains; b: a stepped (S) face contains one; c: a kinked (K) face contains none. Removing a surface atom from an F surface requires breaking the bonds with five nearest neighbors, removing one from an S surface requires breaking four bonds, and removing an atom from a K surface requires breaking

three bonds. For equal bond strengths, the order of their relative radial etch rates is thus: $\boldsymbol{v_R(F)} < \boldsymbol{v_R(S)} < \boldsymbol{v_R(K)}$.

Figure 5. A generalized etched-track model constructed from kinetic principles. a: following removal of its damaged core at a high rate $\boldsymbol{v_T}$, the track can be thought of as a straight channel of unspecified cross-section extending from the surface into the crystal interior; b: in longitudinal cross-section the channel is concave at its lower end and convex at its intersection with the surface; the etched track is therefore bounded by the slowest etching faces at its end and the fastest etching faces at the surface, so developing a distinct channel and etch pit; c: in transverse cross-section, both the etch pit and the track channel are concave and bounded by the slowest etching orientations. Panels b and c are not consecutive etch stages but represent the same final stage with the convexities and concavities parallel (b) and perpendicular (c) to the track shown separately for clarity.

Figure 6. An etch pit at a dislocation emerging at a basal surface of an annealed Durango apatite; annealing conditions: 10 h at 450 °C; etching conditions: 30 min in 0.4 M HNO_3 at 25 °C. According to the kinetic model its edge (A-B) is parallel to the slowest etching orientations (periodic bond chains) in the basal plane, and the etch pit face (A-B-C) is the fastest etching plane hinged on A-B. The hillocks on the etch pit faces support the notion that these are fast etching (Batterman, 1957; Jonckheere and Van den haute, 1996). The absence of hillocks on the smooth basal face, in contrast, confirms that it is slow etching, in accordance with the assumption that it is an F face.

Figure 7. Plot of the radial etch rate $\boldsymbol{v_R}$ as a function of orientation. a: cross-section parallel to a prism plane; b: cross-section parallel to the basal plane. It is assumed that the radial etch rate is minimum perpendicular to the basal and prism planes and maximum at an angle of 30° to the ***c***-axis. Other $\boldsymbol{v_R}$-values in the prism plane are set at the maxima that contribute no additional faces or curvature to the basic etch pit profile; those in the basal plane are based on observation. The dashed line is a modification of the etch rate plot for calculating the track terminations in Figure 12g-i.

Figure 8. Etch rates parallel to basal and prism surfaces of apatite. a: SEM image of a basal surface with a 11.1 MeV/amu ^{132}Xe-ion track parallel to the ***c***-axis, etched for 20 s in 5.5 M HNO_3 at 21 °C; b: etch rate plot derived from the etch-pit outline (A-F) in a; solid sections: calculated values; dashed sections: minimum values; c: SEM image of a prism surface with a 11.1 MeV/amu ^{132}Xe-ion track perpendicular to the surface, etched for 40 s in 5.5 M HNO_3 at 21 °C; d: etch-rate

plot derived from the etch-pit outline (A-F) in c; solid sections: calculated values; dashed sections: minimum values; the solid sections are extended 7.5° to either side of the calculated etch rate vectors for clarity.

Figure 9. Schematic relationship between the faces bounding a track channel and the periodic bond chains. a: a track parallel to the ***c***-axis is bounded by faces containing chains parallel to the prism face (P-P) and to the basal face (B-B); b: a track perpendicular to the ***c***-axis is bounded by a pair of faces containing chains parallel to ***c***-axis (P-P) and a pair containing chains parallel to the basal face (B-B). c: a track at an angle to the ***c***-axis is flanked by a pair of faces containing chains parallel to the ***c***-axis (P-P). The faces containing the P-P chains in b and c can also contain B-B chains, but this is not the case in general. This arrangement accounts for the needle-shaped track channels parallel and perpendicular to the ***c***-axis, and the knife-blade shaped channels of other tracks.

Figure 10. Calculated orthogonal cross-sections of track-surface intersections based on the etch rate plot in Figure 7, and corresponding observations (a-c: basal face; d-f: prism face; g-i: intermediate face). The tracks dip 60° in a plane perpendicular to a basal surface (a, b), a prism surface (d, e), and a surface at 45° to the ***c***-axis (g, h). A-B-C-D: channel determined by the etch rates perpendicular to the track axis; P-Q-R-S: layer removed at the etch rate perpendicular to the surface; X-Y-Z: etch pit determined by the orientation and magnitude of the etch-rate maxima. The right column shows images of etched tracks in apatite exhibiting features predicted by the $\boldsymbol{v_R}$ model. c: SEM image of fission tracks in a basal surface; f: compressed transmitted-light image stack of fission tracks in a prism face; i: SEM image of 11.1 MeV/amu ^{132}Xe tracks perpendicular to a surface inclined at 30° from the prism face. All tracks etched for 20 s in 5.5 M HNO_3 at 21 °C.

Figure 11. a-g: calculated terminations of tracks at increasing angles to the ***c***-axis based on the $\boldsymbol{v_R}$ plot in Figure 7; h-j: calculated terminations of tracks at increasing angles to the ***c***-axis based on a modification of the $\boldsymbol{v_R}$ plot in Figure 7. The modification involves a reduction of the radial etch rates in the angular interval 30-90° to the ***c***-axis. The original values are shown in dashed lines for comparison. The reduced etch rates result in curvature of the track termination parallel to the ***c***-axis.

Figure 12. a-c: calculated intersections of confined tracks parallel to an apatite prism face with a cleavage parallel to the ***c***-axis; azimuth angles to the ***c***-axis: (a) 90°, (b) 75°, and (c) 60°. d-f: etched confined tracks parallel to an apatite prism face, exhibiting features predicted by the $\boldsymbol{v_R}$

model (cf. a-c); etching conditions: 40 s in 5.5 M HNO_3 at 21 °C; azimuth angles: (d) 88°, (e) 85°, (f) 68°.

Figure A1. Calculated cross-sections of track-surface intersections based on the etch rate plot in Figure 7. The track axis lies in a plane perpendicular to a basal surface, and dips 90° to 15° with respect to that surface. The profiles illustrate the persistence of an etch pit of almost constant diameter and depth through a large range of dip angles, and the variation of channel height with dip angle. A-B-C-D and X-Y-Z as explained in Figure 10.

Figure A2. Cross-sections of track-surface intersections based on the etch rate plot in Figure 7. The track lies in a plane perpendicular to a prism surface and parallel to the ***c***-axis, and dips 90° to 15°. The profiles show a distinct etch pit at high angles, which is absorbed in the channel with decreasing dip. A-B-C-D and X-Y-Z as explained in Figure 10.

Figure A3. Cross-sections of track-surface intersections based on the etch-rate plot in Figure 7. The track lies in a plane perpendicular to a surface inclined 45° to the basal face and parallel to the ***c***-axis, and dips 90 to 15°. In most cases, no large etch pit develops due to the high surface etch rate and broad channel, except that a distinct collar develops when the track is parallel to a slow etching plane. A-B-C-D and X-Y-Z as explained in Figure 10. .

654

Figures

Figure 1

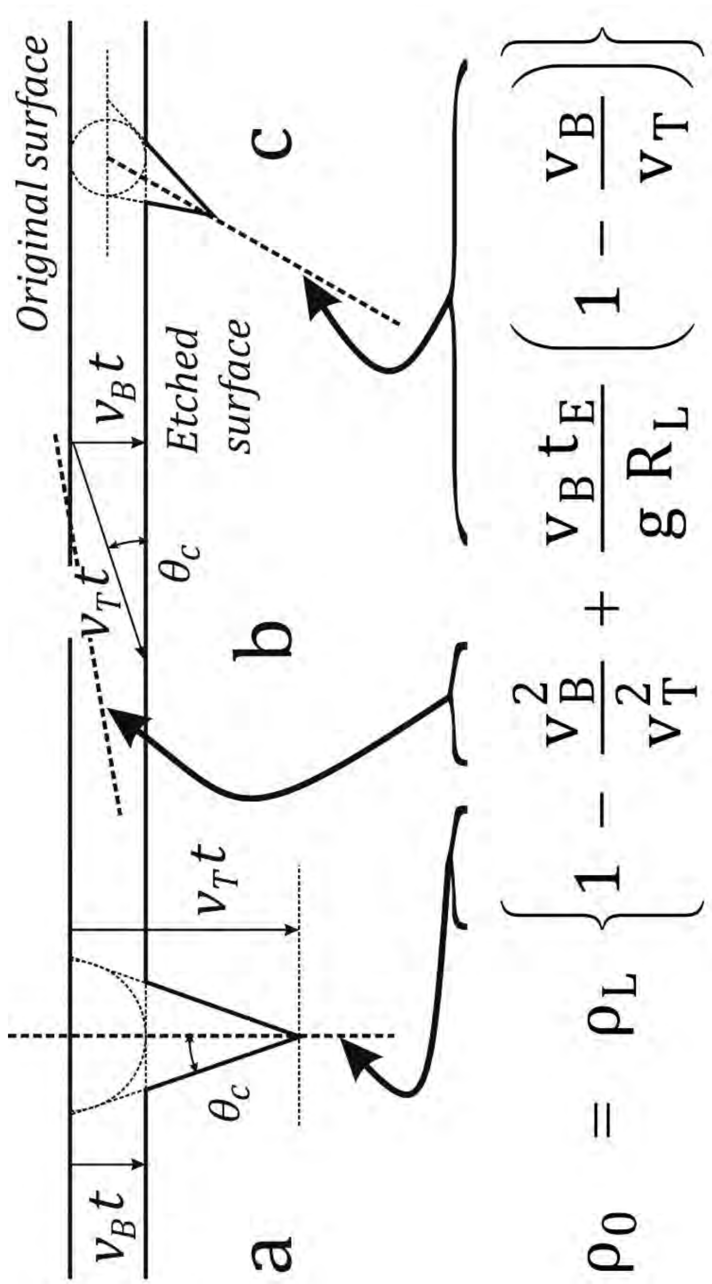

This is a preprint, the final version is subject to change, of the American Mineralogist (MSA)
Cite as Authors (Year) Title. American Mineralogist, in press.
DOI: https://doi.org/10.2138/am-2019-6762

Figure 2

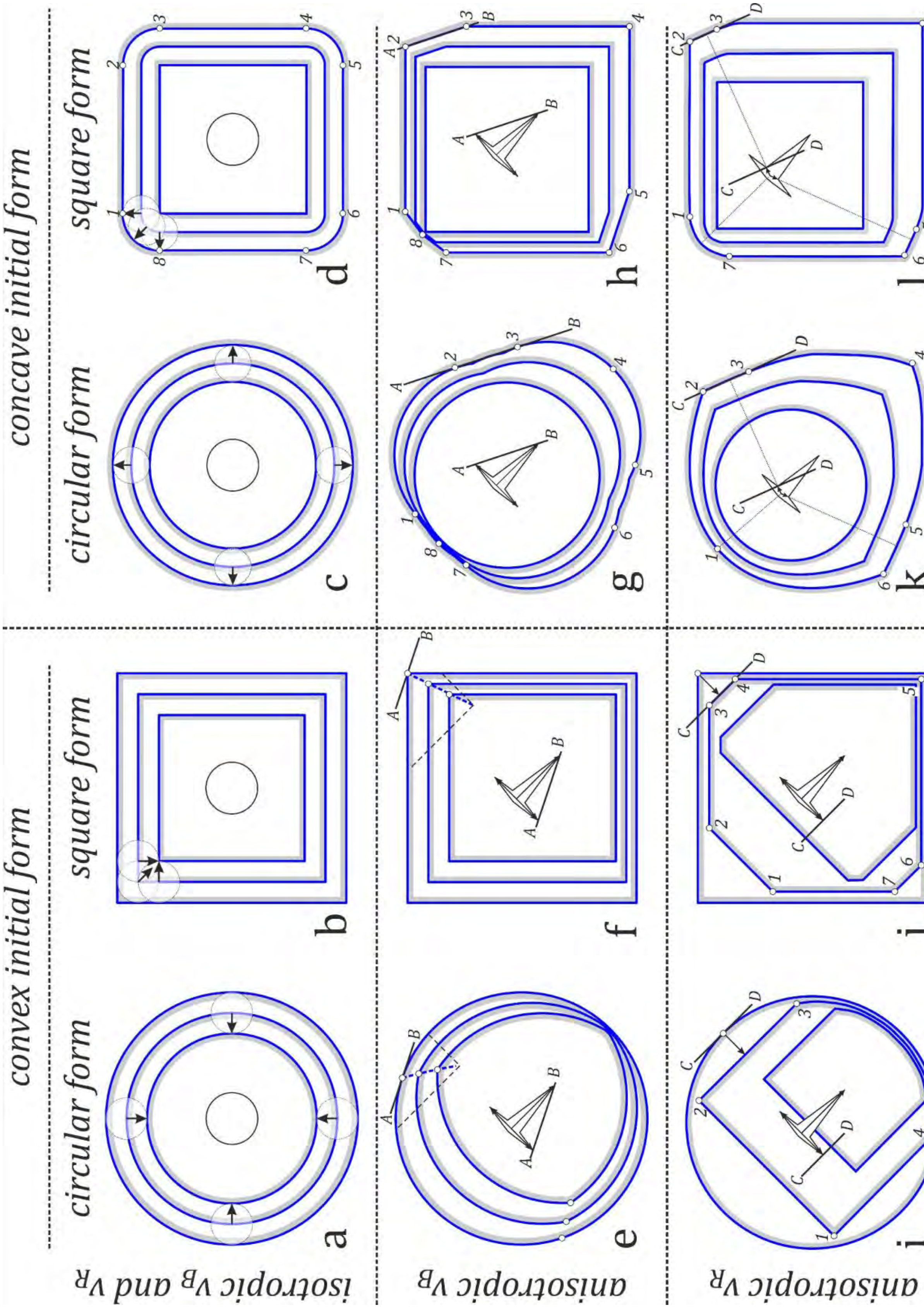

This is a preprint, the final version is subject to change, of the American Mineralogist (MSA)
Cite as Authors (Year) Title. American Mineralogist, in press.
DOI: https://doi.org/10.2138/am-2019-6762

Figure 3

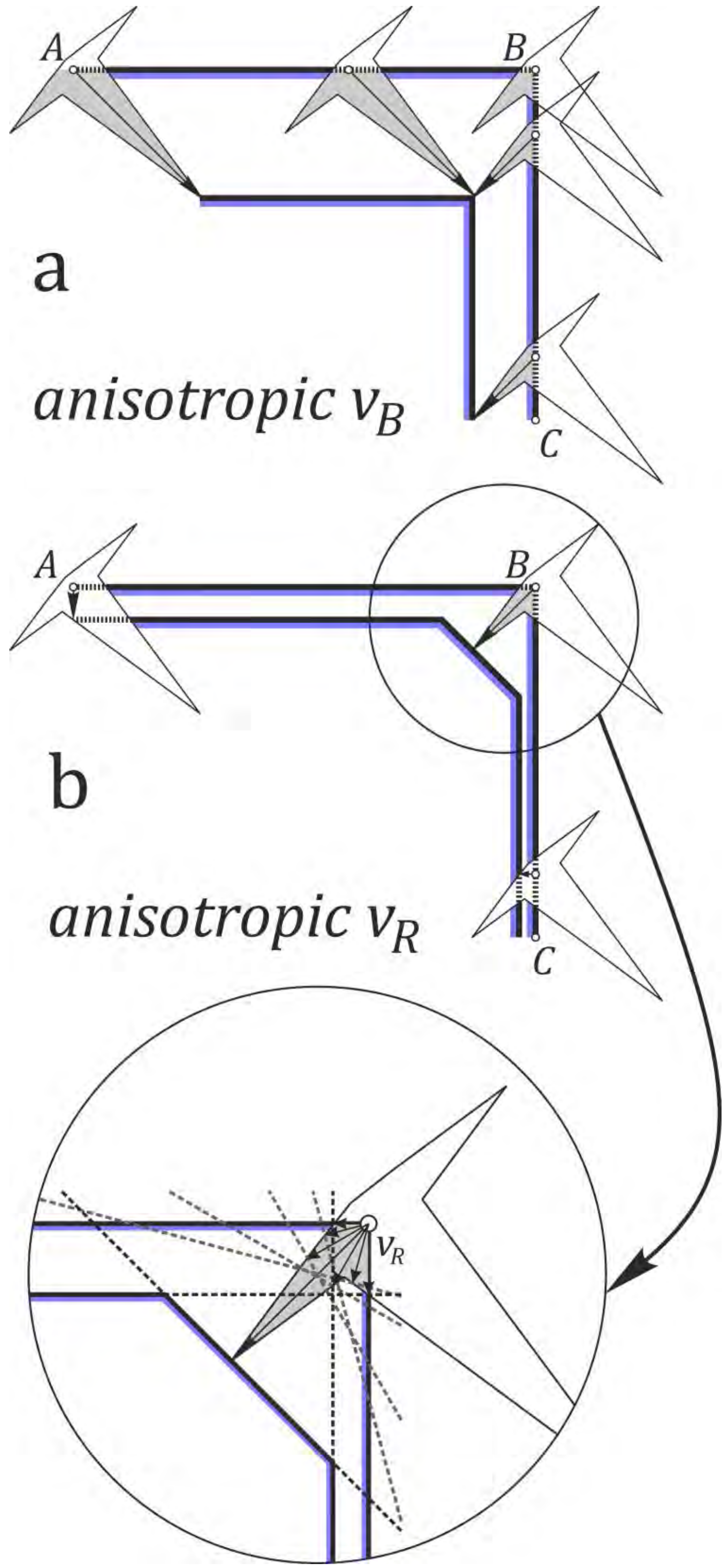

This is a preprint, the final version is subject to change, of the American Mineralogist (MSA)
Cite as Authors (Year) Title. American Mineralogist, in press.
DOI: https://doi.org/10.2138/am-2019-6762

Figure 4

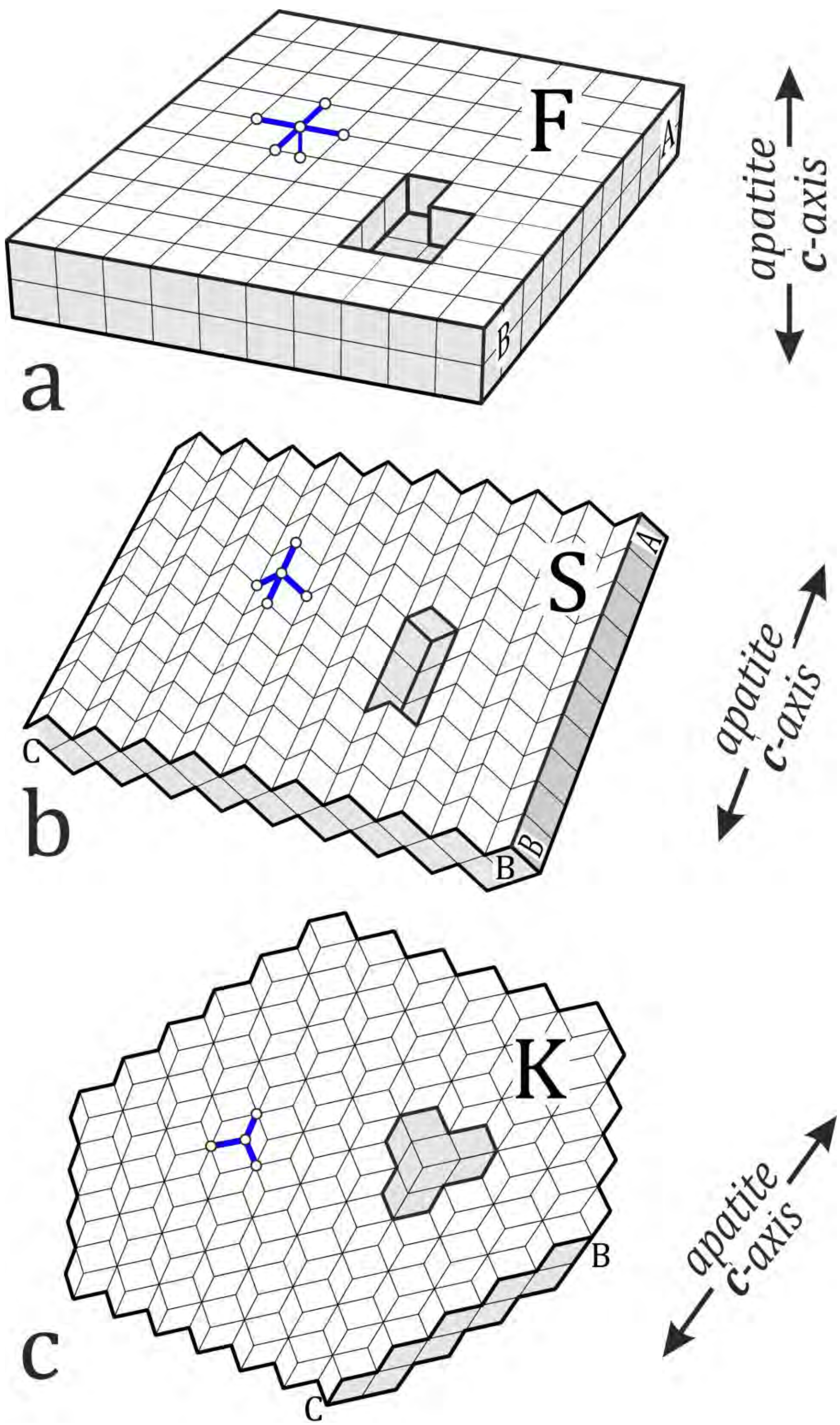

Figure 5

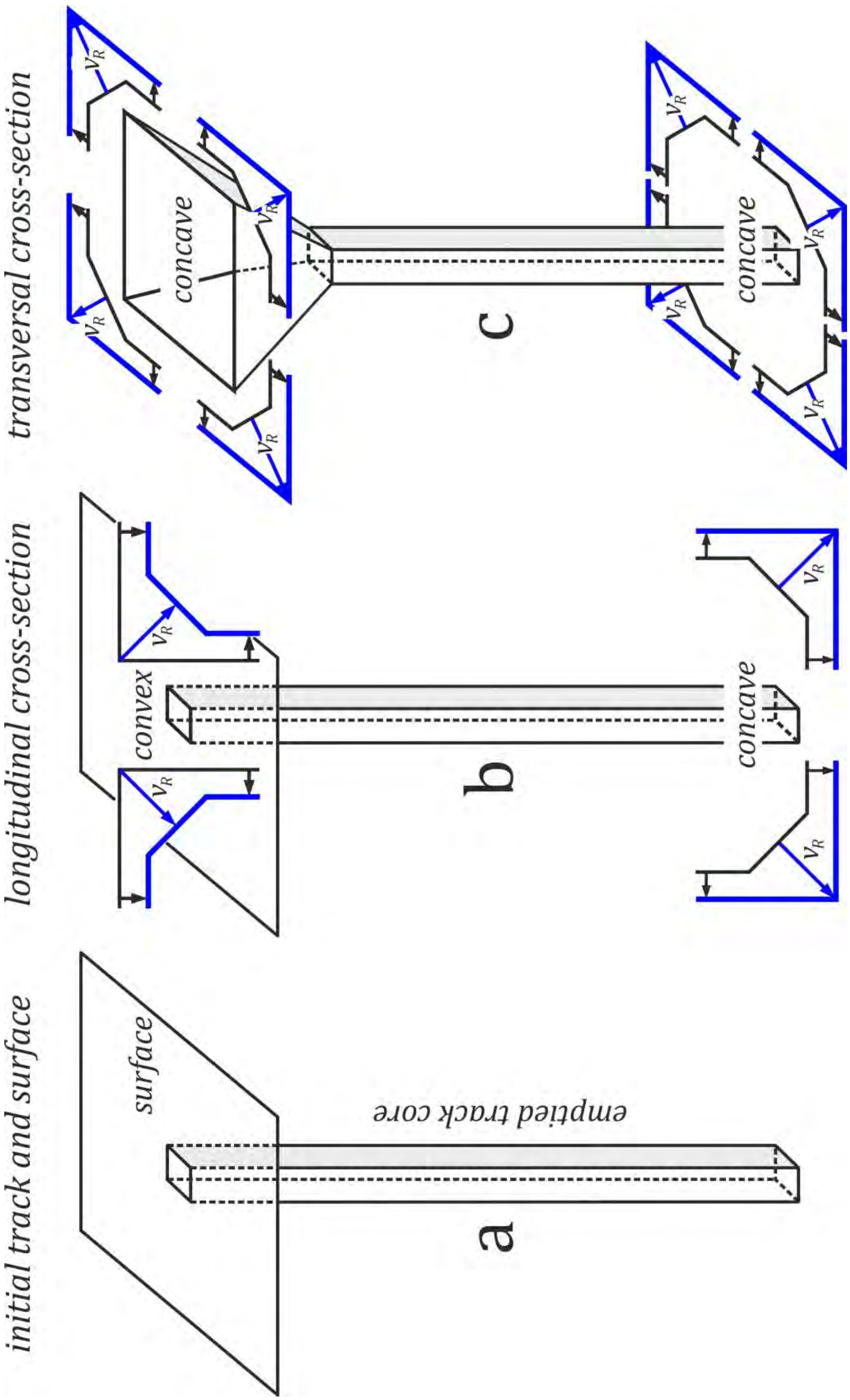
initial track and surface
surface
emptied track core
a
longitudinal cross-section
convex
concave
b
transversal cross-section
concave
concave
c
v_R

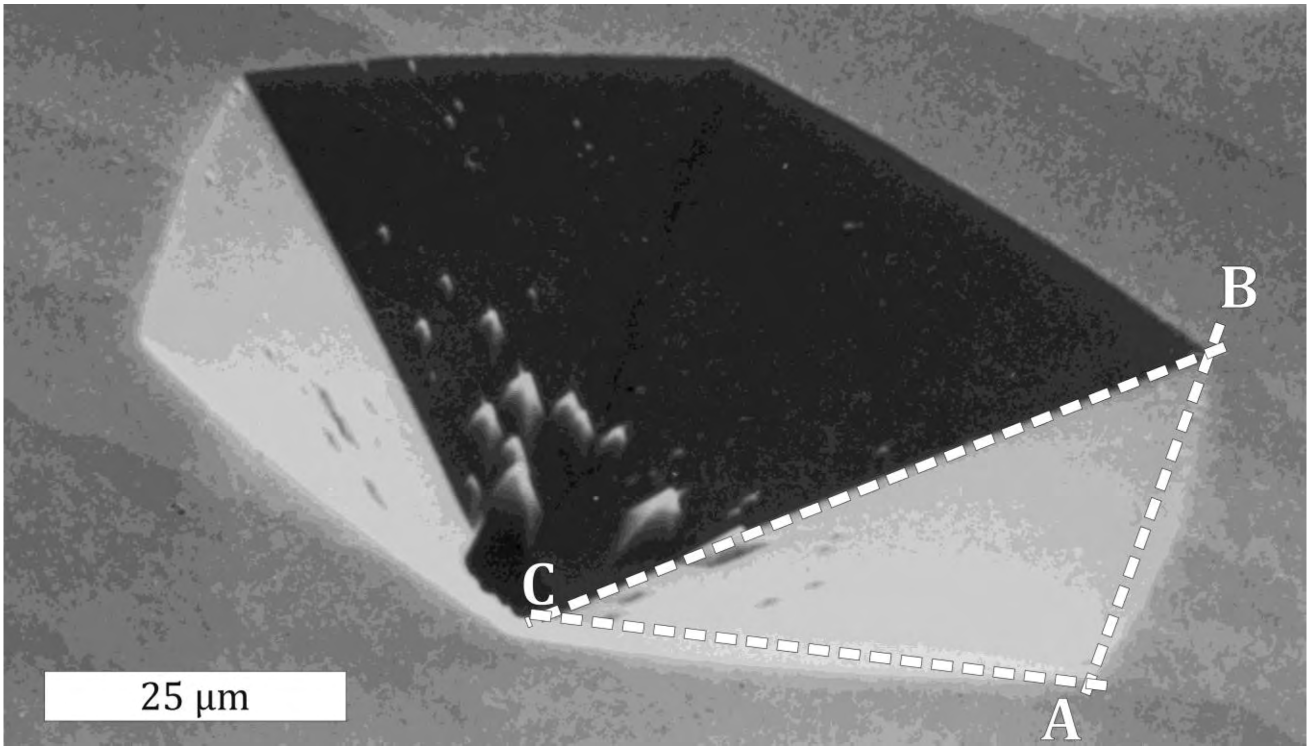

Figure 6

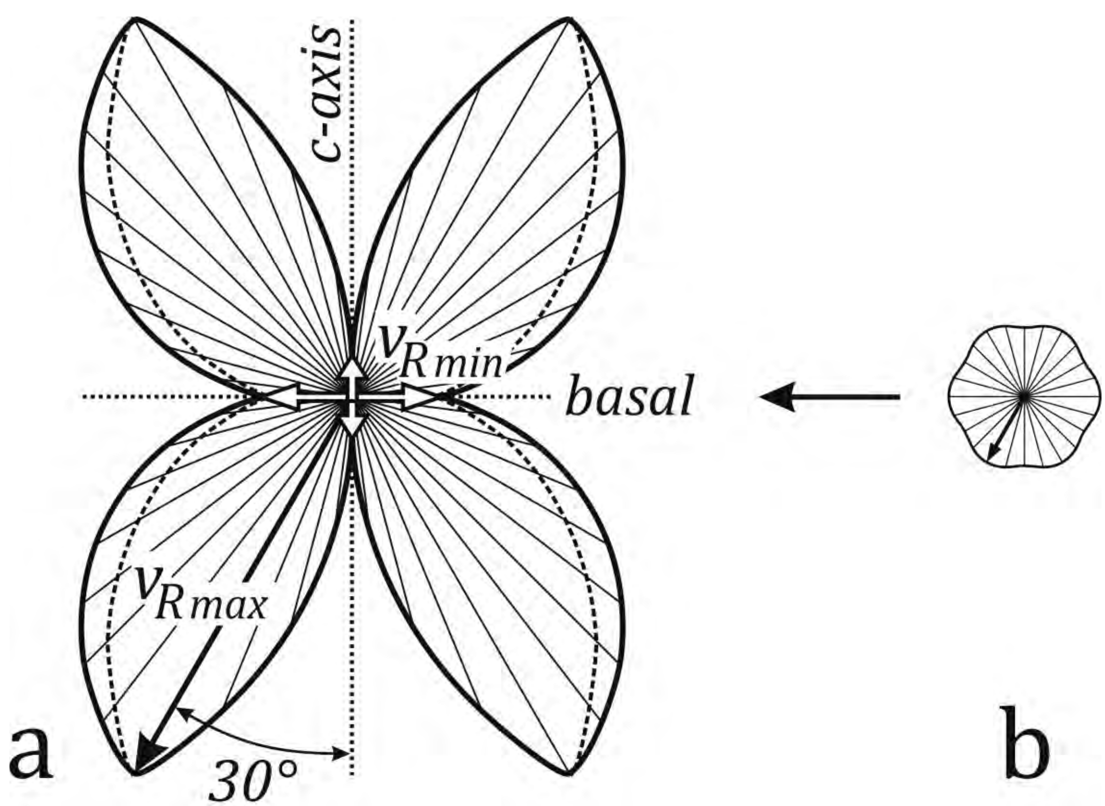

Figure 7

This is a preprint, the final version is subject to change, of the American Mineralogist (MSA)
Cite as Authors (Year) Title. American Mineralogist, in press.
DOI: https://doi.org/10.2138/am-2019-6762

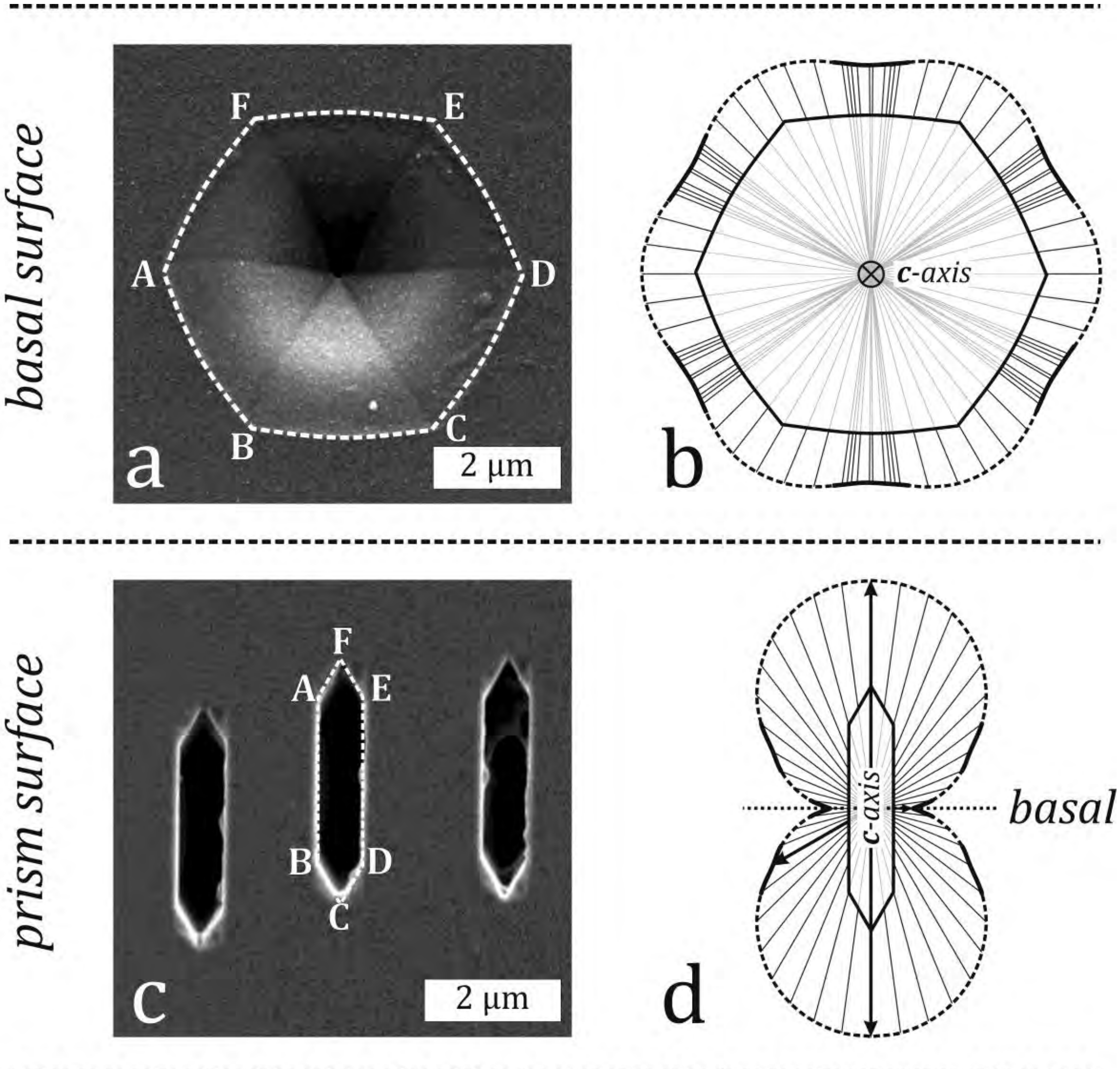

Figure 8

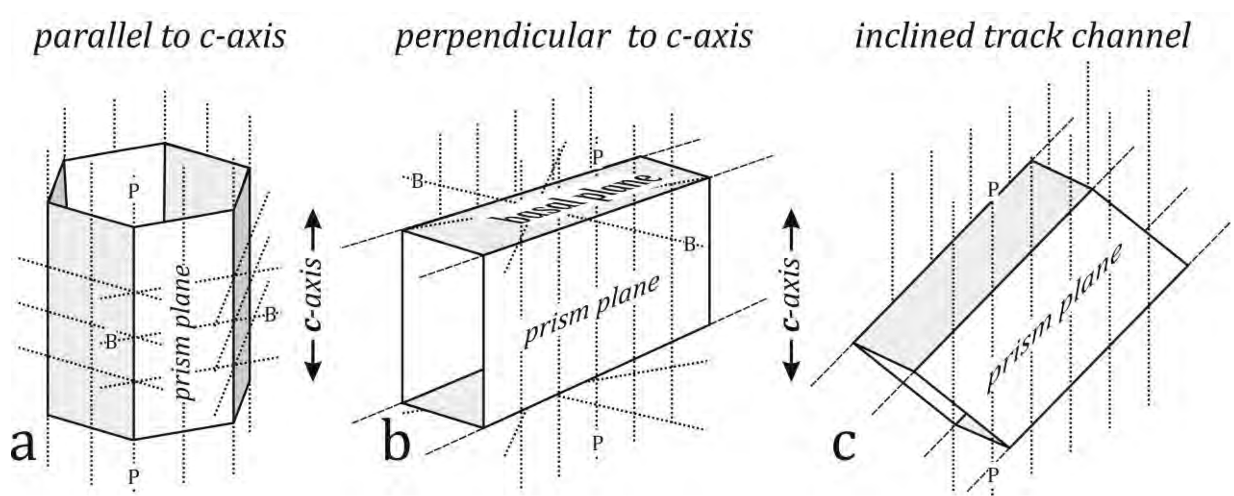

Figure 9

This is a preprint, the final version is subject to change, of the American Mineralogist (MSA)
Cite as Authors (Year) Title. American Mineralogist, in press.
DOI: https://doi.org/10.2138/am-2019-6762

Figure 10

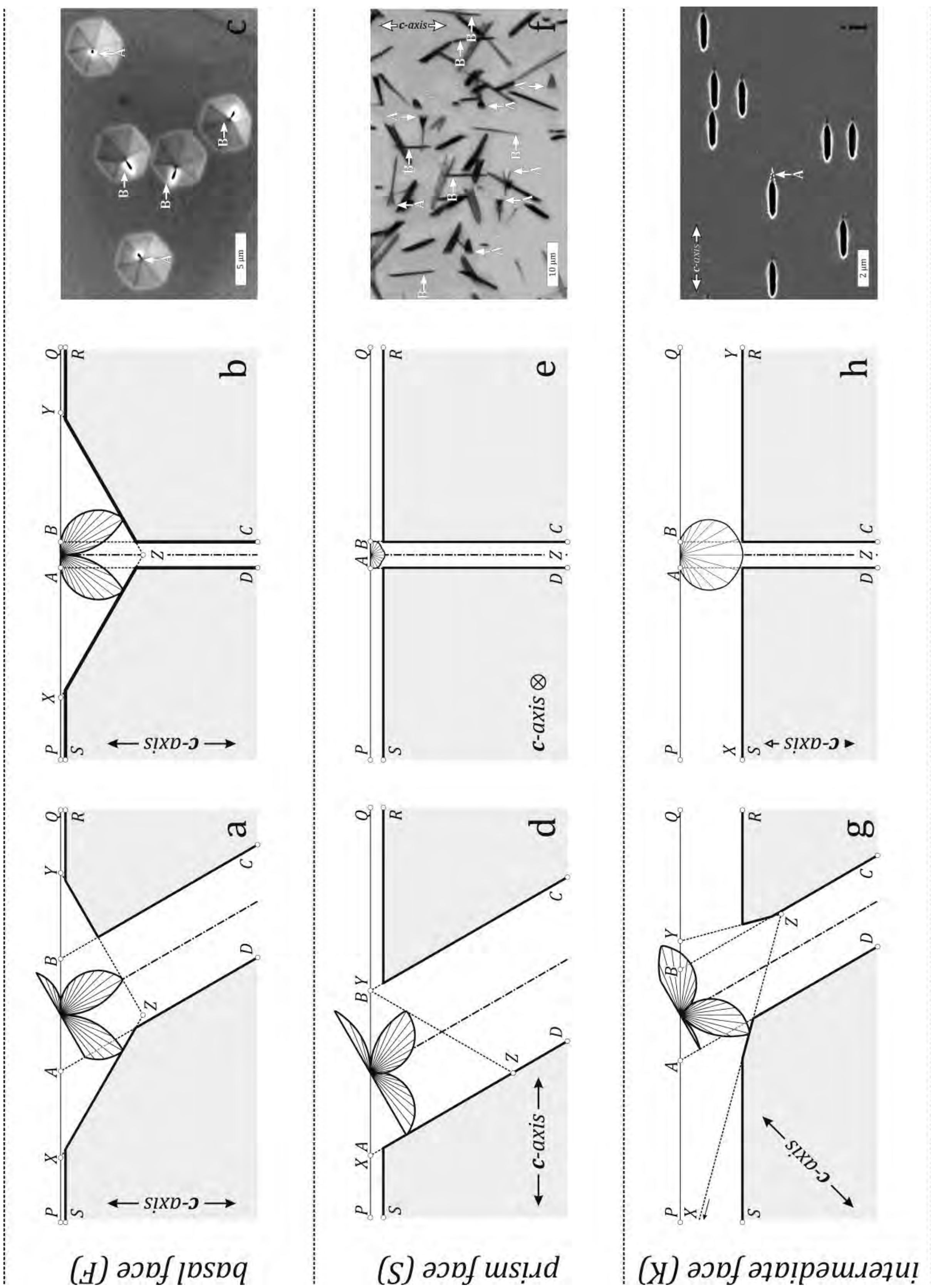

This is a preprint, the final version is subject to change, of the American Mineralogist (MSA)
Cite as Authors (Year) Title. American Mineralogist, in press.
DOI: https://doi.org/10.2138/am-2019-6762

Figure 11

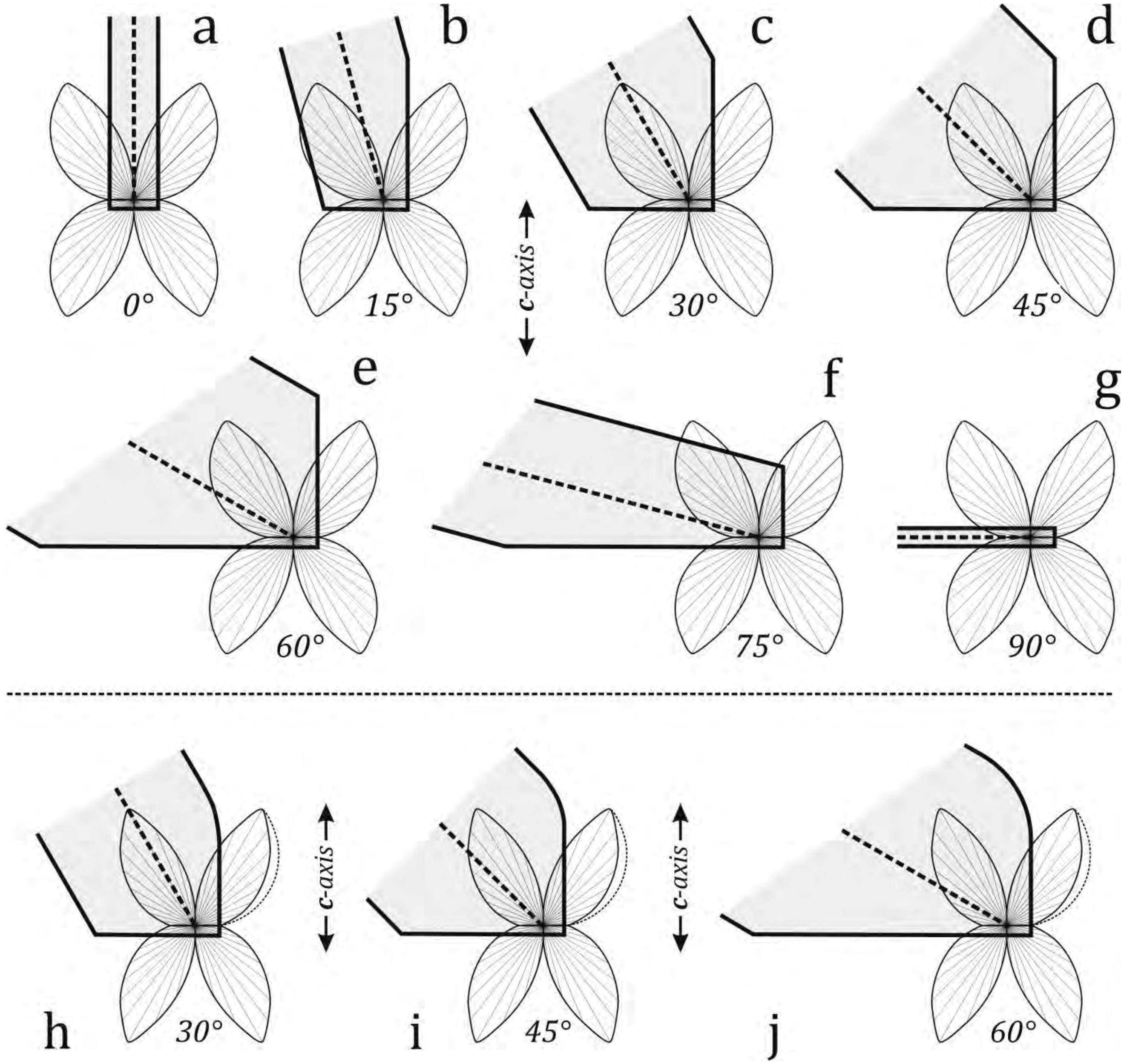

This is a preprint, the final version is subject to change, of the American Mineralogist (MSA)
Cite as Authors (Year) Title. American Mineralogist, in press.
DOI: https://doi.org/10.2138/am-2019-6762

Figure 12